Huygens wavefront tracing: A robust alternative to conventional ray tracing[a]

[a]Published in SEP Report, 95, 101-113 (1997)

Paul Sava and Sergey Fomel[1]

ABSTRACT

We present a method of ray tracing that is based on a system of differential equations equivalent to the eikonal equation, but formulated in the ray coordinate system. We use a first-order discretization scheme that is interpreted very simply in terms of the Huygens' principle. The method has proved to be a robust alternative to conventional ray tracing, while being faster and having a better ability to penetrate the shadow zones.

INTRODUCTION

Though traveltime computation is widely used in seismic modeling and routine data processing, attaining sufficient accuracy without compromising speed and robustness is problematic. Moreover, there is no easy way to obtain the traveltimes corresponding to the multiple arrivals that appear in complex velocity media.

The tradeoff between speed and accuracy becomes apparent in the choice between the two most commonly used methods, ray tracing and numerical solutions to the eikonal equation. Other methods reported in the literature (dynamic programming (Moser, 1991), wavefront construction (Vinje et al., 1993), etc.) are less common in practice (Audebert et al., 1994).

Eikonal solvers provide a relatively fast and robust method of traveltime computations (Vidale, 1990; van Trier and Symes, 1991). They also avoid the problem of traveltime interpolation to a regular grid which imaging applications require. However, the eikonal solvers compute first-arrival traveltimes and lack the important ability to track multiple arrivals. In complex velocity structures, the first arrival does not necessarily correspond to the most energetic wave, and other arrivals can be crucially important for accurate modeling and imaging (Geoltrain and Brac, 1993; Gray and May, 1994).

On the other hand, one-point ray tracing can compute multiple arrivals with great accuracy. Unfortunately, it lacks the robustness of eikonal solvers. Increasing the accuracy of ray tracing in the regions of complex velocity variations raises the cost

[1]**e-mail:** paul@sep.stanford.edu, sergey@sep.stanford.edu

of the method and makes it prohibitively expensive for routine large-scale applications. Mathematically, ray tracing amounts to a numerical solution of the initial value problem for a system of ordinary differential equations (Červený, 1987). These ray equations describe characteristic lines of the eikonal partial differential equation.

Here, we propose a somewhat different approach to traveltime computation, that is both fast and accurate, and has the ability to find multiple arrival traveltimes. The theoretical construction is based on a system of differential equations, equivalent to the eikonal equation, but formulated in the ray coordinate system. Unlike eikonal solvers, our method produces the output in ray coordinates. Unlike ray tracing, it is computed by a numerical solution of partial differential equations. We show that the first-order discretization scheme has a remarkably simple interpretation in terms of the Huygens' principle and propose a *Huygens wavefront tracing* (from now on referred to as *HWT*) scheme as a robust alternative to conventional ray tracing. Numerical examples demonstrate the following properties of the method: stability in media with strong and sharp lateral velocity variations, better coverage of the shadow zones, and greater speed than paraxial ray tracing (from now on referred to as *PRT*).

CONTINUOUS THEORY

The eikonal equation, governing the traveltimes from a fixed source in an isotropic heterogeneous medium, has the form

$$\left(\frac{\partial \tau}{\partial x}\right)^2 + \left(\frac{\partial \tau}{\partial y}\right)^2 + \left(\frac{\partial \tau}{\partial z}\right)^2 = \frac{1}{v^2(x,y,z)} \; . \tag{1}$$

Here x, y, and z are spatial coordinates, τ is the traveltime (eikonal), and v stands for the velocity field. Constant-traveltime contours in the traveltime field $\tau(x,y,z)$, constrained by equation (1) and appropriate boundary conditions, correspond to wavefronts of the propagating wave. Additionally, each point on a wavefront can be parameterized by an arbitrarily chosen ray parameter γ. In three dimensions, γ includes a pair of independent parameters. For brevity, from now on we will restrict the analysis to two dimensions. One can easily generalize it to the 3-D case by considering γ and x as vector quantities. Thus, we will refer to the following two-dimensional form of equation (1):

$$\left(\frac{\partial \tau}{\partial x}\right)^2 + \left(\frac{\partial \tau}{\partial z}\right)^2 = \frac{1}{v^2(x,z)} \; . \tag{2}$$

For a point source, γ can be chosen as the initial ray angle at the source. Zhang (1993) shows that γ as a function of spatial coordinates satisfies the simple partial differential equation

$$\frac{\partial \tau}{\partial x}\frac{\partial \gamma}{\partial x} + \frac{\partial \tau}{\partial z}\frac{\partial \gamma}{\partial z} = 0 \; . \tag{3}$$

Equation (3) merely expresses the fact that in an isotropic medium, rays are locally orthogonal to wavefronts. The field $\gamma(x,z)$ has not only theoretical interest as it

provides one of the possible ways for evaluating propagation amplitudes. In particular, the geometrical spreading factor $J(x,z)$ is connected to γ by the simple relationship (Zhang, 1993)

$$\left(\frac{\partial \gamma}{\partial x}\right)^2 + \left(\frac{\partial \gamma}{\partial z}\right)^2 = \frac{1}{J^2(x,z)} \; . \tag{4}$$

It is important to note that for complex velocity fields, both τ and γ as functions of x and z become multi-valued. In this case, the multi-valued character of the ray parameter γ corresponds to the situation, where more than one ray from the source passes through a particular point $\{x,z\}$ in the subsurface. This situation presents a very difficult problem when equations (2) and (3) are solved numerically. Typically, only the first-arrival branch of the traveltime is picked in the numerical calculation. The ray tracing method is free from that limitation because it operates in the ray coordinate system. Ray tracing computes the traveltime τ and the corresponding ray positions x and z for a fixed ray parameter γ.

Since $x(\tau,\gamma)$ and $z(\tau,\gamma)$ are uniquely defined for arbitrarily complex velocity fields, we can now make an important mathematical transformation. Considering equations (2) and (3) as a system and applying the general rules of calculus, we can transform this system by substituting the inverse functions $x(\tau,\gamma)$ and $z(\tau,\gamma)$ for the original fields $\tau(x,z)$ and $\gamma(x,z)$. The resultant expressions take the form

$$\left(\frac{\partial x}{\partial \tau}\right)^2 + \left(\frac{\partial z}{\partial \tau}\right)^2 = v^2\left(x(\tau,\gamma), z(\tau,\gamma)\right) \tag{5}$$

and

$$\frac{\partial x}{\partial \tau}\frac{\partial x}{\partial \gamma} + \frac{\partial z}{\partial \tau}\frac{\partial z}{\partial \gamma} = 0 \; . \tag{6}$$

Comparing equations (5) and (6) with the original system (2-3) shows that equations (5) and (6) again represent the dependence of ray coordinates and Cartesian coordinates in the form of partial differential equations. However, the solutions of system (5-6) are better behaved and have a unique value for every τ and γ. These values can be computed with the conventional ray tracing. However, the ray-tracing approach is based on a system of ordinary differential equations, which represents a different mathematical model.

We use equations (5) and (6) as the basis of our wavefront tracing algorithm. The next section discusses the discretization of the differential equations and the physical interpretation we have given to the scheme.

A DISCRETIZATION SCHEME AND THE HUYGENS' PRINCIPLE

A natural first-order discretization scheme for equation (5) leads to the difference equation

$$\left(x^i_{j+1} - x^i_j\right)^2 + \left(z^i_{j+1} - z^i_j\right)^2 = \left(r^i_j\right)^2 \; , \tag{7}$$

where the index i corresponds to the ray parameter γ, j corresponds to the traveltime τ, $r^i_j = \triangle\tau\, v^i_j$, $\triangle\tau$ is the increment in time, and v^i_j is the velocity at the $\{i,j\}$ grid point. It is easy to notice that equation (7) simply describes a sphere (or a circle in two dimensions) with the center at $\{x^i_j, z^i_j\}$ and the radius r^i_j. This sphere is, of course, the wavefront of a secondary Huygens source.

This observation suggests that we apply the Huygens' principle directly to find an appropriate discretization for equation (6). Let us consider a family of Huygens spheres, centered at the points along the current wavefront. Mathematically, this family is described by an equation analogous to (7), as follows:

$$(x - x(\gamma))^2 + (z - z(\gamma))^2 = r^2(\gamma)\ . \tag{8}$$

Here the ray parameter γ serves as the parameter that distinguishes a particular Huygens source. According to the Huygens' principle, the next wavefront corresponds to the envelope of the wavefront family. To find the envelop condition, we can simply differentiate both sides of equation (8) with respect to the family parameter γ. The result takes the form

$$(x(\gamma) - x)\ x'(\gamma) + (z(\gamma) - z)\ z'(\gamma) = r(\gamma)r'(\gamma)\ , \tag{9}$$

which is clearly a semidiscrete analog of equation (6). To complete the discretization, we can represent the γ-derivatives in (9) by a centered finite-difference approximation. This representation yields the scheme

$$\left(x^i_j - x^i_{j+1}\right)\left(x^{i+1}_j - x^{i-1}_j\right) + \left(z^i_j - z^i_{j+1}\right)\left(z^{i+1}_j - z^{i-1}_j\right) = r^i_j\left(r^{i+1}_j - r^{i-1}_j\right)\ , \tag{10}$$

which supplements the previously found scheme (7) for a unique determination of the point $\{x^i_{j+1}, z^i_{j+1}\}$ on the i-th ray and the $(j+1)$-th wavefront. Formulas (7) and (10) define an update scheme, depicted in Figure 1. To fill the $\{\tau,\gamma\}$ plane, the scheme needs to be initialized with one complete wavefront (around the wave source) and two boundary rays.

The solution of system (7-10) has the explicit form

$$x^i_{j+1} = x^i_j - r^i_j\left(\alpha\left(x^{i+1}_j - x^{i-1}_j\right) \pm \beta\left(z^{i+1}_j - z^{i-1}_j\right)\right)\ , \tag{11}$$

$$z^i_{j+1} = z^i_j - r^i_j\left(\alpha\left(z^{i+1}_j - z^{i-1}_j\right) \mp \beta\left(x^{i+1}_j - x^{i-1}_j\right)\right)\ , \tag{12}$$

where

$$\alpha = \frac{r^{i+1}_j - r^{i-1}_j}{\left(x^{i+1}_j - x^{i-1}_j\right)^2 + \left(z^{i+1}_j - z^{i-1}_j\right)^2}\ , \tag{13}$$

(14)

and

$$\beta = \mathrm{sign}\left(x^{i+1}_j - x^{i-1}_j\right)\frac{\sqrt{\left(x^{i+1}_j - x^{i-1}_j\right)^2 + \left(z^{i+1}_j - z^{i-1}_j\right)^2 - \left(r^{i+1}_j - r^{i-1}_j\right)^2}}{\left(x^{i+1}_j - x^{i-1}_j\right)^2 + \left(z^{i+1}_j - z^{i-1}_j\right)^2}\ . \tag{15}$$

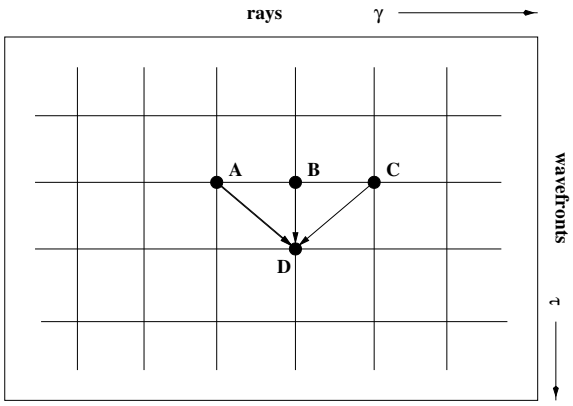

Figure 1: An updating scheme for HWT. Three points on the current wavefront (A, B, and C) are used to advance in the τ direction.

Figure 2 shows a geometric interpretation of formulas (7) and (10). Formula (10) is clearly a line equation. Thus, the new point D in Figure 2 is defined as one of the two intersections of this line with the B sphere, defined by formula (7). It is easy to show geometrically that the newly created ray segment BD is orthogonal to the common tangent of spheres A and C. Within the finite-difference approximation, the common tangent reflects local wavefront behavior.

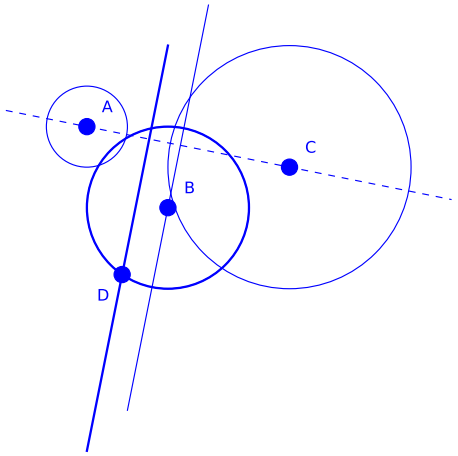

Figure 2: A geometrical updating scheme for HWT in the physical domain. Three points on the current wavefront (A, B, and C) are used to compute the position of the D point. The bold lines represent equations (7) and (10). The tangent to circle B at point D is parallel to the common tangent of circles A and C.

IMPLEMENTATION DETAILS

There are a few problems that have to be addressed for the successful implementation of the algorithm described in the preceding section. The most important are the boundary values, the existence of a double solution (7-10), and the complications of finding the solution in the vicinity of the cusp points.

Boundary values

As mentioned in the preceding section, the application of formulas (11-12) requires the existence of known boundary values for both the first value of τ (next to the wave source) and the extreme values of the take-off angle γ. Therefore, we have to initialize the complete first wavefront as well as two boundary rays that represent all the extreme points of each consequent wavefront (that is, for the first and last considered take-off angle).

To initialize the points on the first wavefront, we consider that the velocity is constant around the source, and therefore this wavefront becomes a circle centered at the source. This is a reasonable assumption because we use a finite difference scheme with very small time steps, and the velocity models have limited local variation.

The values of the boundary rays are externally supplied. This apparent problem is very easy to solve by using a ray tracing program to compute the trajectories of these two boundary rays. We can shoot several "trial" rays and select the ones that are the smoothest and that penetrate the most into the model.

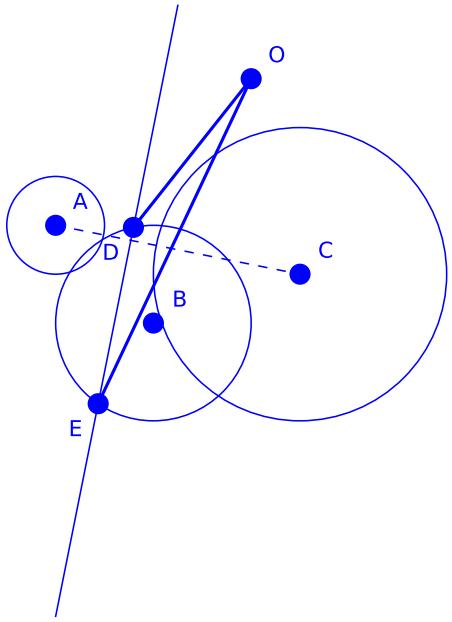

Figure 3: The double solution of the system of equations (7-10). D and E are the intersection points between the circle given by equation (7) and the line given by equation (10). Point O is the previous point on the ray going through B. The distance (OE) is smaller than the distance (OD) and, therefore, D is the next selected point. The middle ray is defined locally by the succession of points (-O-B-D-).

The double solution

The system (7-10) has two theoretical solutions (11-12), though there is only one that makes physical sense given a velocity map. Again, we used a geometrical argument to select the appropriate solution. We observed that even though a wavefront can make a sharp turn, the corresponding rays cannot (see the examples in the next section). We define a turn as "sharp" if it happens over a very small number of samples (say,

three). Consequently, we decided to impose the condition that the correct solution is the one represented by the point farthest away from the preceding one on the same ray (Figure 3).

Cusp Points

The final problem to be solved is represented by the cusp points, the case in which the three-point scheme doesn't provide a satisfactory solution because it tends to decrease in an unnatural way the sharpness of the wavefronts. In this case, we reduce the three-point scheme to a two-point one by assuming that one of the exterior points (either A or C, Figure 4) is merged with the point in the middle (B).

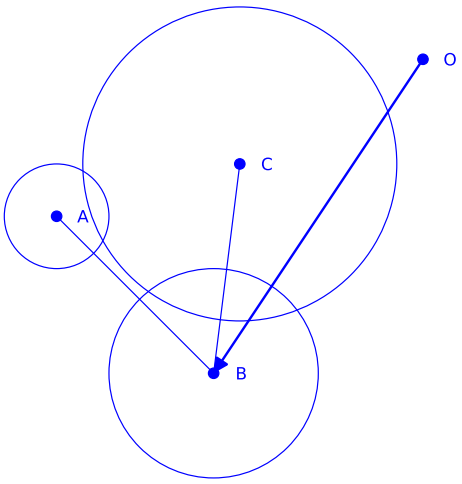

Figure 4: Cusp points. A, B and C are the three points on the current wavefront. Point O is the previous point on the ray going through B. The angle CBA is smaller than the angle OBA, and therefore B is a cusp point. If the angle CBA is closer to 90 degrees than the angle OBA, then C is merged with B; otherwise, A is merged with B. The three-point scheme becomes a two-point scheme without any change in the program.

EXAMPLES

This section presents three examples in which we applied the method described in the last section. The first two applications are on simple Gaussian velocity anomalies in a medium of constant velocity. We used these models to check the validity, accuracy, and stability of the HWT method. The third example concerns the very complex Marmousi 2-D model, which is one of the most difficult benchmarks for ray tracing methods. Throughout the test, we have compared our results with those obtained with a ray tracing program for accuracy, speed, and stability.

Gaussian velocity anomalies

Our first two examples are Gaussian velocity anomalies (one positive and one negative) with a magnitude of 2.0 km/s in a constant velocity medium of 2.0 km/s for the positive anomaly, shown in Figure 5, and of 3.0 km/s for the negative anomaly in

Figure 6. The anomaly is centered at a depth of 1.0km and has a half-width of 300 m. The source is placed on the surface directly above the anomaly (at x=6.0 km).

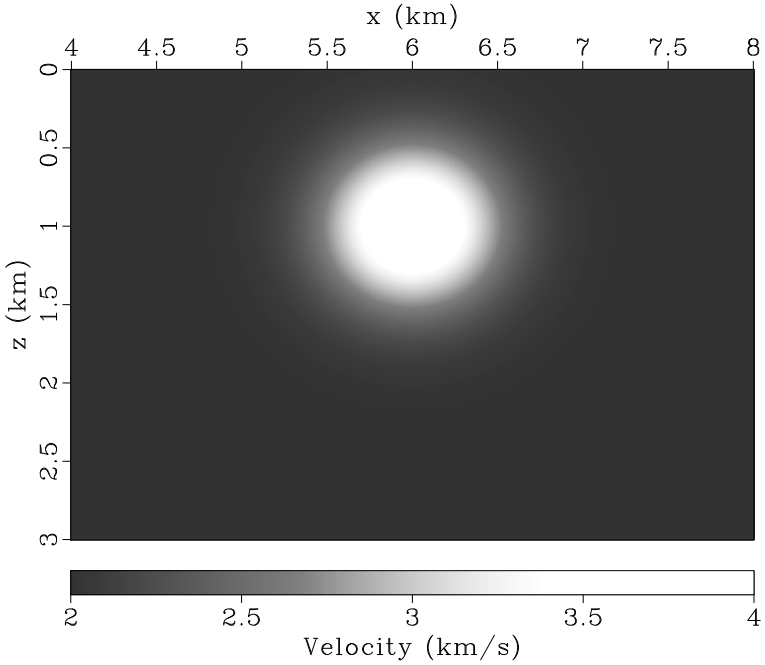

Figure 5: A Gaussian positive velocity anomaly. The background velocity is 2.0 km/s, and the maximum anomaly at the center is +2.0 km/s.

We have selected these velocity models to test the way our method applies to different patterns of velocity variation. In the case of the negative anomaly, the rays focus inward, while in the case of the positive anomaly the rays spread outward.

The distribution of rays as obtained with the PRT and HWT methods are presented in Figure 7 for the positive anomaly, and in Figure 8 for the negative.

One way to compare the two methods is to compute the distance between the points that correspond to the same ray, identified by the same take-off angle, at the same traveltimes. This is obviously not a perfect quantitative comparison, because once two rays, obtained with the two methods, become slightly divergent, they keep going in different directions, and thus the distance between corresponding points keeps growing (Figures 9 and 10). However, this effect is not necessarily a manifestation of decreasing precision. It can be easily seen that if such an angular mismatch doesn't occur, the rays maintain practically the same path (see, for example, the rays shot in the (-20,-40) and (20,40) degree intervals, where the distance decreases in many cases to almost zero). Even in the case of divergent rays, the distance is kept to a reasonable level (less than 1%). Consequently, we do not interpret these differences as error.

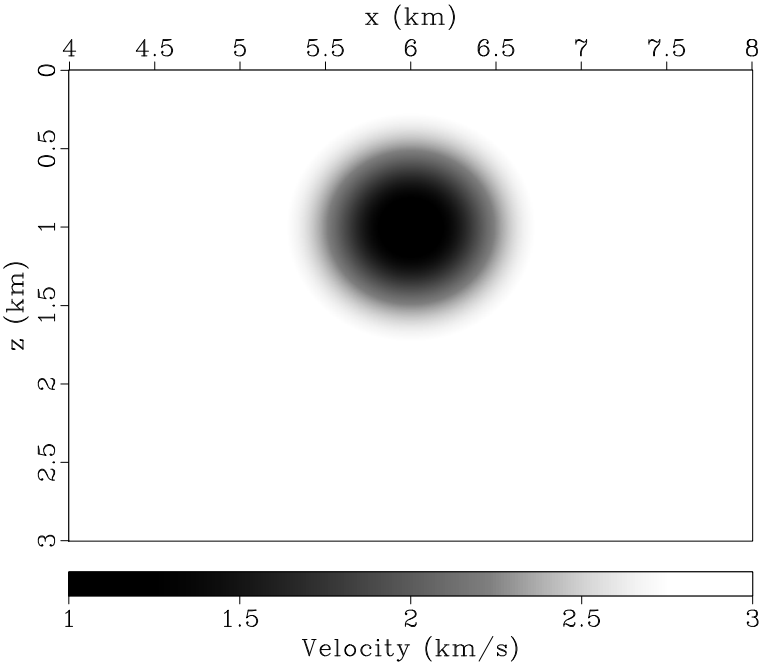

Figure 6: A Gaussian negative velocity anomaly. The background velocity is 3.0 km/s, and the maximum anomaly at the center is -2.0 km/s.

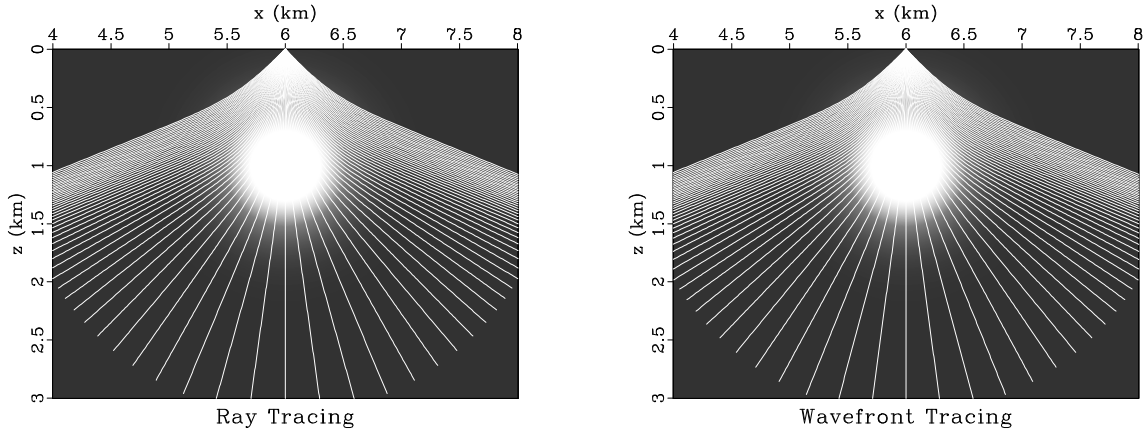

Figure 7: The rays obtained in the case of the Gaussian positive velocity anomaly. We present the rays obtained with the PRT method (left) and with the HWT method (right). The source is located on the surface at x=6.0 km.

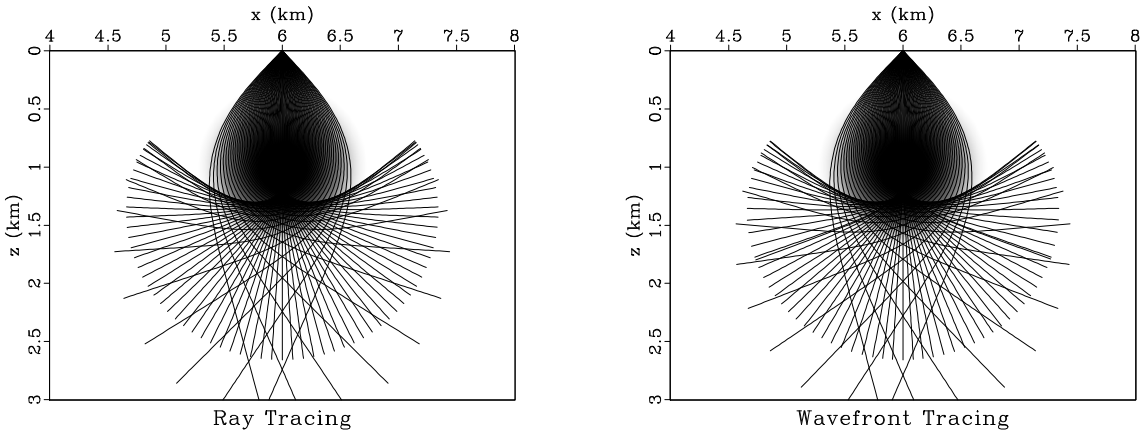

Figure 8: The rays obtained in the case of the Gaussian negative velocity anomaly. We present the rays obtained with the PRT method (left) and with the HWT method (right). The source is located on the surface at x=6.0 km.

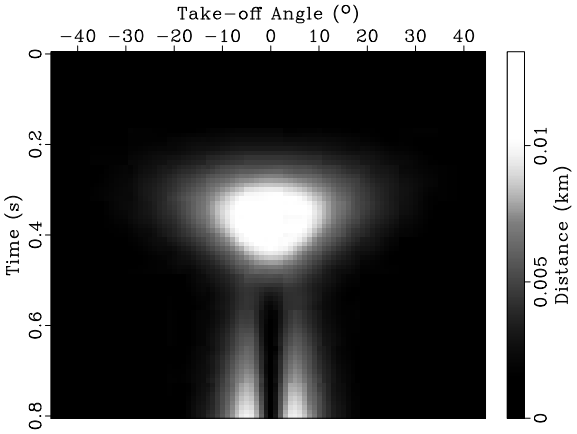

Figure 9: The distance between the corresponding points on the rays obtained with the PRT method and with the HWT method. Distances are given in meters.

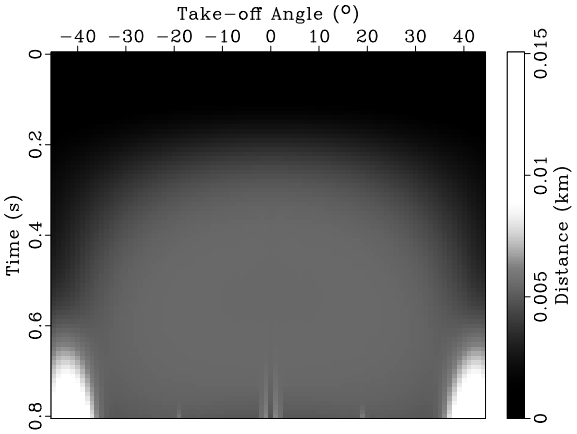

Figure 10: The distance between the corresponding points on the rays obtained with the PRT method and with the HWT method. Distances are given in meters.

The Marmousi model

In the third example, we have applied the same method to trace rays in the far more complex Marmousi 2-D Model. Figure 11 contains the true velocity (left) and a smoothed version using twice a tridiagonal 5×5 filter (right). In Figure 12 we present the rays obtained on the unsmoothed Marmousi Model with the PRT method (left) and with the HWT method (right). In Figure 13 we present the rays obtained on the smoothed Marmousi Model with the PRT method (left) and with the HWT method (right).

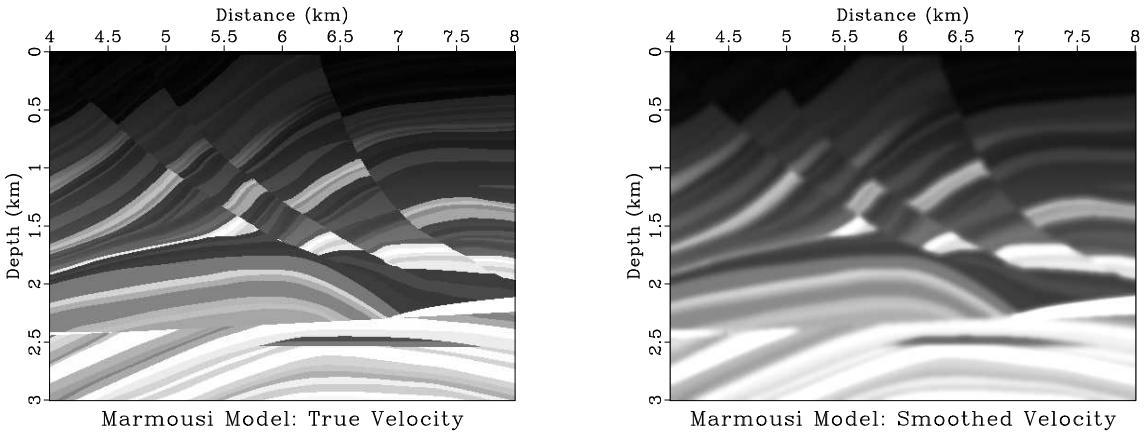

Figure 11: The Marmousi model. The true velocity appears on the left,the smoothed velocity on the right.

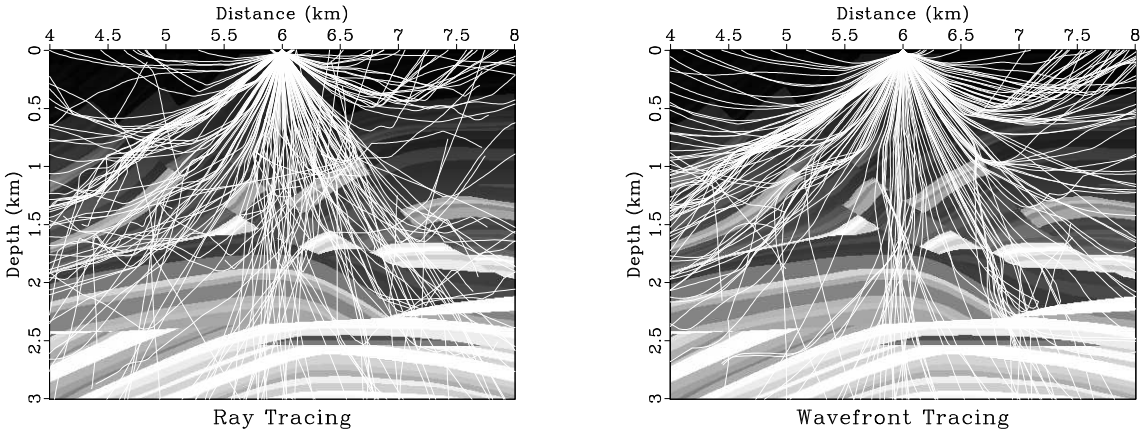

Figure 12: The rays obtained in the true velocity Marmousi model using the PRT method (left) and the HWT method (right).

As expected, the rays traced using the PRT method (Figure 12, left), which represents a more exact solution to the eikonal equation for the given velocity field, have a very rough distribution. Since this erratic result is of no use in practice,

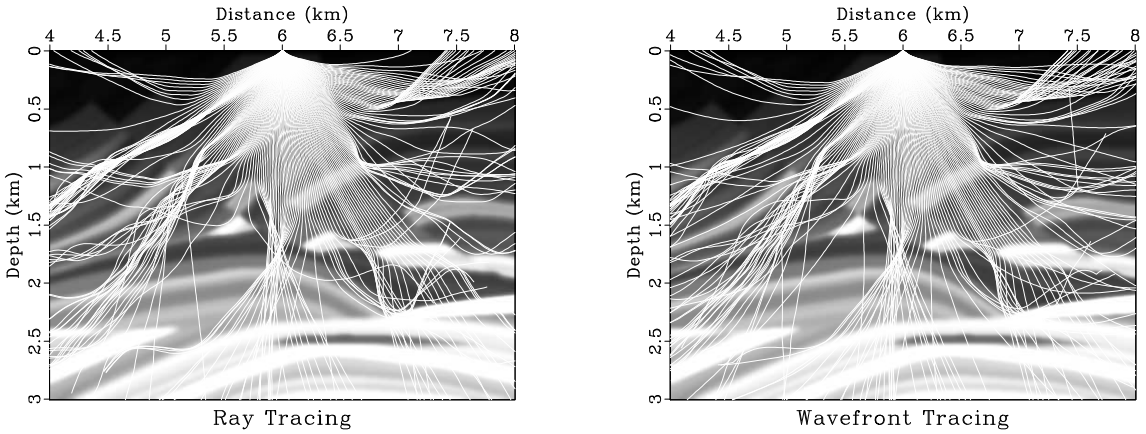

Figure 13: The rays obtained in the smoothed Marmousi model using the PRT method (left) and the HWT method (right).

regardless of its accuracy, the only way to get a proper result is to apply the ray tracing to a smoothed velocity model (Figure 13, left).

On the other hand, the result obtained with the HWT method looks a lot better, though some imperfections are still visible. For the case of the unsmoothed velocity medium, the rays have a much smoother pattern, which is less dependent on how rough the velocity model is (Figure 12, right). This feature is preserved in the case of the smoothed model (Figure 13, right) where the distributions of rays displayed by the two methods are much more similar, though some differences remain (see, for example the zone around x=6.5km, z=2.0km).

As with the Gaussian model, we present the distances between the points that correspond to the same ray, identified by the same take-off angle, at the same traveltimes (Figure 14). This is another way to interpret what we saw in Figure 13, where most of the rays have a consistent behavior, displaying similar paths regardless of the method used, and therefore small distances, and a few have a different trajectory, resulting in big distances that increase with traveltime.

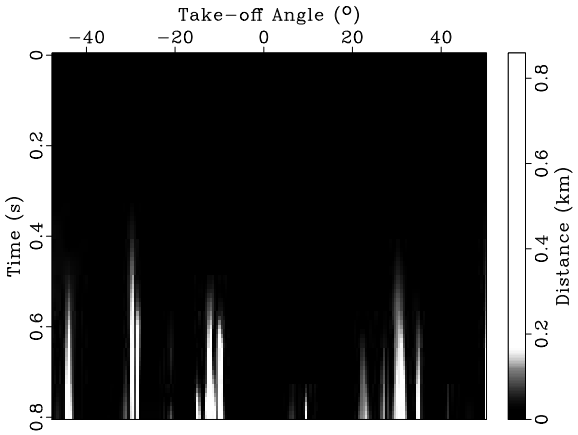

Figure 14: The distance between the corresponding points on the rays obtained with the PRT method and with the HWT method. Distances are given in meters.

CONCLUSIONS

The results obtained so far have led us to the following conclusions:

1. Stability: The HWT method is a lot more stable in rough velocity media than the PRT method. The increased stability results from the fact that HWT derives the points on the new wavefronts from three points on the preceding wavefront, compared to only one in the usual PRT, which also means that a certain degree of smoothing is already embedded in the method. This feature allows us to use the HWT method in media of very sharp velocity variation and still obtain results that are reasonable from a geophysical point of view.

2. Coverage: Being more stable and giving smoother rays than the PRT method, enables the HWT method to provide a better coverage of the shadow zones. The idea is that since the wavefront is traced from one ray to the other, it is very easy to introduce in the code a condition to decrease the shooting angle as soon as the wavefront length exceeds a specified upper limit.

3. Speed: Both methods were tested on an SGI 200. The execution time for shooting 90 rays of 130 samples for each ray was 1.31s for the PRT method and 0.22 s for the HWT method. Even though in the current implementation of HWT we do not compute the amplitudes of the waves, our method has still yielded a big improvement in speed for the 2-D case, which gives us hope of doing even better in the 3-D case.

In our future work, we will implement the 3-D Huygens wavefront tracing method. We expect to preserve its stability, while making it run even faster in comparison to other conventional 3-D ray tracing methods.

REFERENCES

Audebert, F., D. Bevc, B. Biondi, D. Lumley, D. Nichols, G. Palacharla, T. Rekdal, and H. Urdaneta, 1994, Review of traveltime computation methods, *in* SEP-80: Stanford Exploration Project, 25–46.

Červený, V., 1987, Ray tracing algorithms in three-dimensional laterally varying layered structures, *in* Seismic Tomography: Riedel Publishing Co., 99–134.

Geoltrain, S., and J. Brac, 1993, Can we image complex structures with first-arrival traveltime?: Geophysics, **58**, 564–575.

Gray, S. H., and W. P. May, 1994, Kirchoff migration using eikonal equation traveltimes: Geophysics, **59**, 810–817.

Moser, T. J., 1991, Shortest path calculation of seismic rays: Geophysics, **56**, 59–67.

van Trier, J., and W. W. Symes, 1991, Upwind finite-difference calculation of traveltimes: Geophysics, **56**, 812–821.

Vidale, J. E., 1990, Finite-difference calculation of traveltimes in three dimensions: Geophysics, **55**, 521–526.

Vinje, V., E. Iversen, and H. Gjoystdal, 1993, Traveltime and amplitude estimation using wavefront construction: Geophysics, **58**, 1157–1166.

Zhang, L., 1993, Imaging by the wavefront propagation method: PhD thesis, Stanford University.